

Article

Nanostructured MoS₂ and WS₂ Photoresponses under Gas Stimuli

Mohamed A. Basyooni ^{1,2}, Shrouk E. Zaki ^{1,3}, Nada Alfryyan ⁴, Mohammed Tihthi ⁵, Yasin Ramazan Eker ^{6,*}, Gamal F. Attia ⁷, Mücahit Yılmaz ², Şule Ateş ⁸ and Mohamed Shaban ^{9,10,*}

- ¹ Department of Nanotechnology and Advanced Materials, Graduate School of Applied and Natural Science, Selçuk University, Konya 42030, Turkey
- ² Department of Nanoscience and Nanoengineering, Institute of Science and Technology, University of Necmettin Erbakan, Konya 42060, Turkey
- ³ Theoretical Physics Department, National Research Center, Cairo 12622, Egypt
- ⁴ Department of Physics, College of Sciences, Princess Nourah bint Abdulrahman University, P.O. Box 84428, Riyadh 11671, Saudi Arabia
- ⁵ Institute of Ceramics and Polymer Engineering, University of Miskolc, H-3515 Miskolc, Hungary
- ⁶ Department of Metallurgy and Material Engineering, Faculty of Engineering and Architecture, Necmettin Erbakan University, Konya 42060, Turkey
- ⁷ Department of Solar and Space Research, National Research Institute of Astronomy and Geophysics (NRIAG), Cairo 11421, Egypt
- ⁸ Department of Physics, Faculty of Science, Selçuk University, Konya 42075, Turkey
- ⁹ Department of Physics, Faculty of Science, Islamic University of Madinah, P.O. Box 170, AlMadinah Almonawara 42351, Saudi Arabia
- ¹⁰ Nanophotonics and Applications Laboratory, Physics Department, Faculty of Science, Beni-Suef University, Beni-Suef 62514, Egypt
- * Correspondence: yeke@erbakan.edu.tr (Y.R.E.); mssfadel@aucegypt.edu (M.S.)



Citation: Basyooni, M.A.; Zaki, S.E.; Alfryyan, N.; Tihthi, M.; Eker, Y.R.; Attia, G.F.; Yılmaz, M.; Ateş, Ş.; Shaban, M. Nanostructured MoS₂ and WS₂ Photoresponses under Gas Stimuli. *Nanomaterials* **2022**, *12*, 3585. <https://doi.org/10.3390/nano12203585>

Academic Editors: Andrea Orsini and Stefano Salvatori

Received: 25 August 2022

Accepted: 30 September 2022

Published: 13 October 2022

Publisher's Note: MDPI stays neutral with regard to jurisdictional claims in published maps and institutional affiliations.



Copyright: © 2022 by the authors. Licensee MDPI, Basel, Switzerland. This article is an open access article distributed under the terms and conditions of the Creative Commons Attribution (CC BY) license (<https://creativecommons.org/licenses/by/4.0/>).

Abstract: This study was on the optoelectronic properties of multilayered two-dimensional MoS₂ and WS₂ materials on a silicon substrate using sputtering physical vapor deposition (PVD) and chemical vapor deposition (CVD) techniques. For the first time, we report ultraviolet (UV) photoresponses under air, CO₂, and O₂ environments at different flow rates. The electrical Hall effect measurement showed the existence of MoS₂ (n-type)/Si (p-type) and WS₂ (P-type)/Si (p-type) heterojunctions with a higher sheet carrier concentration of $5.50 \times 10^5 \text{ cm}^{-2}$ for WS₂ thin film. The IV electrical results revealed that WS₂ is more reactive than MoS₂ film under different gas stimuli. WS₂ film showed high stability under different bias voltages, even at zero bias voltage, due to the noticeably good carrier mobility of $29.8 \times 10^2 \text{ cm}^2/\text{V}$. WS₂ film indicated a fast rise/decay time of 0.23/0.21 s under air while a faster response of 0.190/0.10 s under a CO₂ environment was observed. Additionally, the external quantum efficiency of WS₂ revealed a remarkable enhancement in the CO₂ environment of 1.62×10^8 compared to MoS₂ film with 6.74×10^6 . According to our findings, the presence of CO₂ on the surface of WS₂ improves such optoelectronic properties as photocurrent gain, photoresponsivity, external quantum efficiency, and detectivity. These results indicate potential applications of WS₂ as a photodetector under gas stimuli for future optoelectronic applications.

Keywords: two-dimensional material; MoS₂; WS₂; thin film; optoelectronics

1. Introduction

Photodetectors have a wide range of applications in the fields of biomedical sensing, environmental monitoring, optical communications, and space exploration. It is well known that photodetector responsivity is mainly dependent on the device material, structure, and operating conditions in terms of bias voltage, temperature, and wavelength of the incident radiation. It thus becomes crucial to have a thorough understanding of the effects of these parameters for designing and fabricating an optimal photodetector [1]. Nowadays, space

has become a new and rich field, as well as a preferential development sector, which is rapidly contributing to countries' financial welfare and progress. Space technologies play a key role in accelerating countries' development processes and increasing societies' quality of life and security. Aerospace and space applications require the development of sensors that are operated in several different environments. Future aeronautical systems will need to be more capable, perform better, and be safer, all of which will require less maintenance. Space sensors and detector application areas include optical, photodetector, leak detection, high temperature, emissions monitoring, fire detection, environmental monitoring, and radiation detection. Each of these detectors is the subject of effort throughout NASA to improve safety and decrease the cost of space travel, significantly reduce the number of emissions produced by aeronautic engines, and improve the safety of commercial airline travel. Testing the performance of the photodetectors under different gas environments is essential to understand their performances under various gas stimuli. For instance, CO₂ is considered one of the primary gases in the space environment and the greenhouse gases in the Earth's atmosphere [2–4]. The Martian atmosphere is primarily composed of 96% CO₂ with a balance of nitrogen, argon, and trace species [5]. There is a highly significant need for testing the performance of optoelectronic devices under different gas environments, such as CO₂, for space and commercial applications.

The exotic physical characteristics of 2D transition metal dichalcogenides (TMDC), such as their non-zero bandgap and layer-dependent second-order optical nonlinearity, are garnering a lot of interest. The chemical formula MX₂ refers to a class of inorganic 2D layered materials where M is a transition metal (typically M = Mo, W, Ti, V, Ta, Hf, and Pt) and X is a group of VI chalcogen atom (typically X = S, Se, and Te). The advantages of both materials are that they can be combined by forming heterojunctions with silicon using 2D layered materials. By being completely compatible with conventional integrated circuit fabrication techniques, it streamlines the manufacturing process; because they have a bandgap of 2 eV in monolayer form. MoS₂ and WS₂ are the most studied materials in the TMDC family [6]. WS₂ is more desirable for optical, electrical, and optoelectronic applications due to its novel properties, including high thermal stability and a wide range of operating temperatures [7], layer-dependent tunable bandgap (1.4–2.1 eV) [8], broad UV-visible absorption spectrum [9], and tunable photoluminescence (PL) effect [10–12].

Graphene, WS₂, MoS₂, and other materials can be produced into 2D sheets using “top-down” techniques like exfoliation methods. Among these, micromechanical exfoliation [13], sonication-assisted liquid exfoliation [14–16], shear exfoliation [17,18], and chemical exfoliation [19,20] have been studied and suggested in the literature. However, they have several disadvantages, such as low quality and small-scale production, many flaws, and a short-range during micromechanical exfoliation [21]. Additionally, transferring the exfoliated layer to a new substrate is required, which makes scaling up and large-scale production more difficult [22]. For this reason, chemical vapor deposition (CVD) with a bottom-up process is preferred during the synthesis of MoS₂ [23,24]. MoO₃ substrate is maintained in the downstream gas flow during growth [25–27]. Thin-film properties like homogeneity and grain size are strongly dependent on MoO₃ substrate properties. Nowadays, the creation of wafer-scale and homogeneous 2D materials has attracted great attention due to the advancement of the following generation of optoelectronic applications and quantum computers. Atomic layer deposition (ALD) [22,28], pulsed laser deposition (PLD) [29,30], thermal evaporation [31–33], and magnetron sputtering systems [34–36] are commonly used for the preparation of MoO₃ substrates. However, magnetron sputtering is the most preferred, since its low cost and ease of control are suitable for large-scale commercial manufacturing. MoO₃ is sulfurized within a two or three-zone quartz tube under an Ar inert atmosphere via sublimation of sulfur powders. Similar processes are used with WO₃ to grow WS₂ TMDC.

WS₂ and MoS₂ are two TMDC thin films that have tunable optical bandgaps, making them promising for photodetection applications. A suitable structure may be sensitive to an incident light involving a photocurrent whose intensity is compared to the current under

darkness (dark current) [37]. Photoconduction and photogate are two major effects that contribute to photocurrent [38]. The process of photoconduction happens when free charge carriers are absorbed by light with photon energy greater than the MoS₂ (or WS₂) bandgap. The highest photo responsiveness occurs when all photons are absorbed and each input photon produces one electron and one hole. This indicates that the primary photoresponse mechanism in MoS₂ (or WS₂) phototransistors is a photogate, in which light absorption introduced a change in the trapped charges density. When photogate occurs in the MoS₂ (or WS₂) thin film, the threshold voltage V_{TH} , the gate voltage separating the high-current (ON) and low-current (OFF) regimes, shifts as a result of trapped charges causing a change in the effective gate voltage, which introduces a great increase in current [39].

Gas adsorption can affect the Fermi-level energy of MoS₂ [40]; therefore, several investigations on 2D TMDC-based photodetectors and gas sensors have been conducted [41]. The effect of O₂, N₂, and Ar on the optoelectronic rGO performance was studied [42]. As with n-type rGO, oxidizing gases such as O₂, CO₂, and N₂ pull electron clouds from the n-type semiconductor sheets, resulting in a drop in charge carriers and an increase in resistance [42,43]. Different compounds have also been tested, such as the effect of the atmosphere on the device performance of perovskite solar cells during operation. Indeed, Guo et al. [44] investigated the degradation mechanisms of perovskite solar cells operated under a vacuum and a nitrogen atmosphere.

According to our investigations, there is no complete work related to the study of the effect of CO₂ gas adsorptions on MoS₂ and WS₂ by examining and comparing photodetection parameters. To fabricate MoS₂ and WS₂-based optoelectronic photodetector sensors, PVD layers of molybdenum and tungsten oxide were deposited on silicon substrates, then sulfurization occurred in a CVD chamber. The effect of different gas adsorptions, such as air, O₂, and CO₂, on MoS₂ and WS₂ thin films, were investigated in this work. In addition, their optoelectronic performance under UV illumination is discussed in detail.

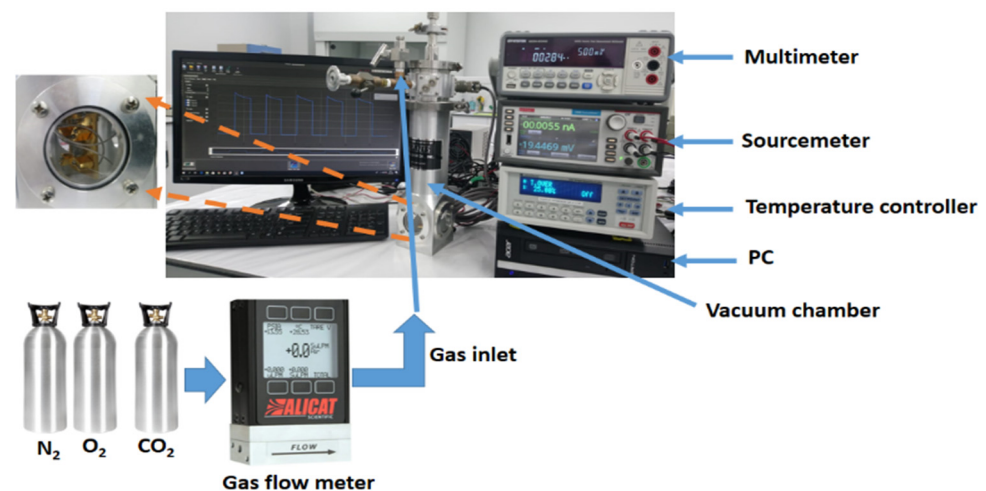
2. Materials and Fabrication Methods

2.1. Fabrication of Thin Films

The fabrication process of MoS₂ and WS₂ thin films is similar to the previously reported studies [45,46]. The advantage of this process is to increase film homogeneity and scalability. This method also demands that there are no small discounted triangular-like shapes of MoS₂ or WS₂, as known for the CVD deposition process of 2D materials. MoS₂ and WS₂ thin films were prepared on a p-type silicon substrate first by using a PVD system, which included an RF magnetron sputtering system followed by a CVD process. Substrates of Si were cleaned in a series of steps, firstly a 5 min dip in an NH₄OH-H₂O₂ solution watered down with pure water at 75 °C. Then, they were put in a 5% HF solution for 5 s, after which they were washed in pure water and dried with N₂. The Si substrates were put into the RF magnetron sputtering system right away. To activate the Si surface, a 100 W Ar-plasma source was opened for 10 min at room temperature. Targets made of tungsten and molybdenum were used as the primary sources, with Ar plasma serving as the carrier gas and O₂ as the reactive gas. The substrate temperature was kept under control at 400 °C for more than 30 min, increasing by 100 °C/30 min. We maintained constant O₂ and Ar flow rates. The films were deposited at 5E-3 Torr and 137 W using 30 s sputtering times. Before being moved to the two-zone CVD quartz chamber for the sulfurization process, the system was naturally cooled to room temperature. In the center of the CVD furnace, the temperature of the Mo-O and W-O thin films as they were being deposited was elevated to 650–750 °C. A 100 sccm Ar source was used with a ceramic boat that contained 0.5 g sulfur powder. An external heating belt was used to evaporate the sulfur for 25 min at a distance of 50 cm from the substrate. The system then cooled until it reached RT while receiving an Ar flow rate of 100 sccm.

2.2. Characterization Techniques

Field-emission scanning electron microscopy (FE-SEM; Zeiss Gemini 500, Cambridge, UK) was used to record the surface morphology. The topography and line profile spectrum were examined using atomic force microscopy (AFM, Park, Santa Clara, CA, USA) Park XE7 system via noncontact mode through a $1 \times 1 \mu\text{m}$ scanning area and a tip scan speed of 1 Hz. XEI 4.3.4 2016 data processing and analysis software (Park, Santa Clara, CA, USA) were used to measure the roughness values. In addition, confocal Raman microscopy was utilized to introduce thin film optical images. X-ray photoelectron spectroscopy (XPS) measurements were investigated based on the Thermo Scientific K-alpha XPS system (Thermo Scientific™, Waltham, MA, USA) using an Al K_{α} source and a spot size of 400 μm . Photoluminescence (PL) and Raman vibrational modes were performed using Renishaw inVia confocal Raman microscope (Renishaw, New Mills, UK) with a laser beam of a wavelength value of 532 nm. SWIN Hall8800 Hall Effect measurement system is employed to measure the carrier's concentration and mobility. The electrical I-V and optoelectronics measurements were carried out using Tektronix Keithley 2400 Sourcemeter (20 mV and 10 nA sensitive, Tektronix, Beaverton, OR, USA) through a four-probe system and KickStart Keithley software (Tektronix, Beaverton, OR, USA) for data acquisitions. A 365 nm ultraviolet (UV, Konya, Turkey) light lamp was used for illumination. The same calculations and measurements can be reported under different gas (such as CO_2) and temperature environments by using a stain steel vacuum chamber with a quartz window, as shown in Scheme 1. The system has a quartz window that can be used to transmit light into the sample easily under temperature or gas environments. The temperature can be controlled with a Lake Shore Model 335 Cryogenic Temperature Controller (Woburn, MA, USA). These measurements were repeated under high-purity gases of O_2 , CO_2 , and N_2 to study the stimuli effects. Here, the role of N_2 was just to clean/stabilize the environment around the photodetector sample. Since we were using different gases (CO_2 and O_2), cleaning the environment around the sample with a vacuum and inert gas (N_2) was necessary. The gases are controlled with the Alicat Scientific Mass flow meter MC model. All the measurements were recorded and captured from the computer, and after that, the analyses were carried out.



Scheme 1. Electrical and optoelectrical systems under different gas environments and different temperature conditions.

3. Results and Discussion

3.1. Raman and PL Spectra

The Raman spectra of 2D materials show characteristics of two main peaks with E_{2g}^1 and A_{1g} modes. According to the literature, Mo-S atoms vibrate in the plane at $E_{2g}^1 = 382.01 \text{ cm}^{-1}$ while S atoms oscillate perpendicular to the plane at $A_{1g} = 407 \text{ cm}^{-1}$,

as shown in Figure 1a [23,24,47]. Concerning WS_2 , E_{2g}^1 and A_{1g} modes, the peaks are located at 354.08 and 420.09 cm^{-1} , respectively. The differences between E_{2g}^1 and A_{1g} for MoS_2 and WS_2 are 23.76 and 66.01 cm^{-1} , respectively. These results show the existence of multilayered MoS_2 and WS_2 structures of a few nanometers in size, as has been reported before [24,45,48].

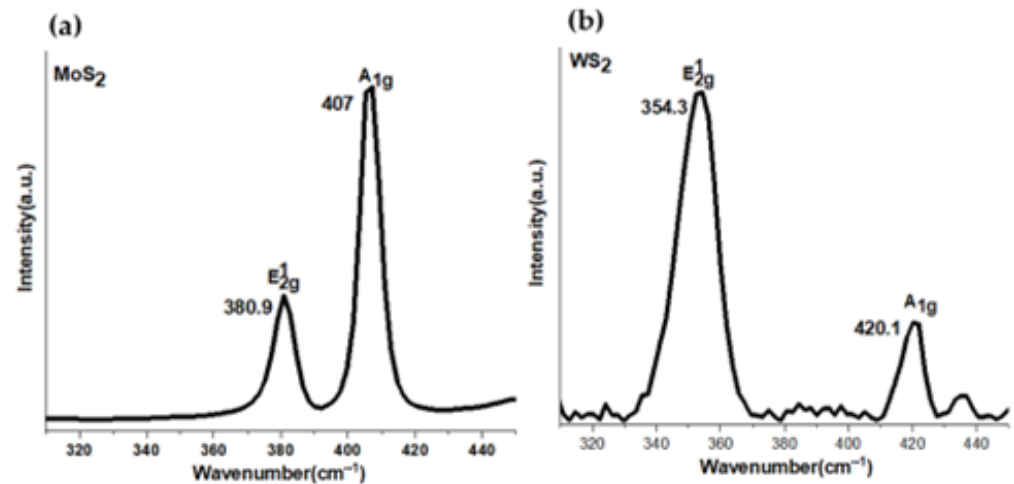


Figure 1. (a,b) Raman spectra of MoS_2 and WS_2 on Si substrates, respectively.

From the measurements of photoluminescence (PL), it can be seen that the thin films introduced a direct and indirect electronic band transition. MoS_2 's optical properties are greatly influenced by the number of layers. The energies of direct excitonic transitions have a substantial PL effect in monolayer MoS_2 , but this effect is reduced due to the layer's number increasing and completely disappearing in bulk MoS_2 . The PL spectra of MoS_2 are observed at 610 and 624 nm (Figure 2a). These peaks are related to direct excitonic transitions at the Brillouin zone of the K point and represent the A and B excitation of MoS_2 [49]. Furthermore, photogenerated electron-hole pair recombination is attributed to the prominent peak at 682 nm, while the valence band separated as the MoS_2 's high spin-orbit coupling is attributed to the lesser peak at 624 nm [50]. Nevertheless, the trion exhibits localized quasiparticles with negative (two electrons with one hole) and positive (two holes with one electron) charges as PL peaks at 682 nm. According to the report, the monolayer introduced a strong peak at 615 nm (2.02 eV) that was associated with the A exciton resonance. It is believed that at the K point, the direct exciton transition between the maximum of the valence band and the minimum of the conduction band (CBM) is what causes the PL in the monolayer [51]. However, the bilayer and trilayer PL spectra show wider and lower energy emissions than those of the indirect exciton, in which the VBM is still at the K point but the CBM is located between the K point and the peaks [52]. For WS_2 , two peaks at 612 and 700 nm are observed (Figure 2b).

3.2. Surface Morphology and Topography

Large-scale MoS_2 thin films have been previously worked on by combining CVD and sputtering techniques [53]. Optical microscopy was used to capture the MoS_2 and WS_2 surfaces, as seen in Figure 3a,b, respectively. At a macroscopic scale, the texture of WS_2 is more homogeneous than that of MoS_2 . The structural domains of WS_2 are smaller than those of MoS_2 (see Figure 3b).

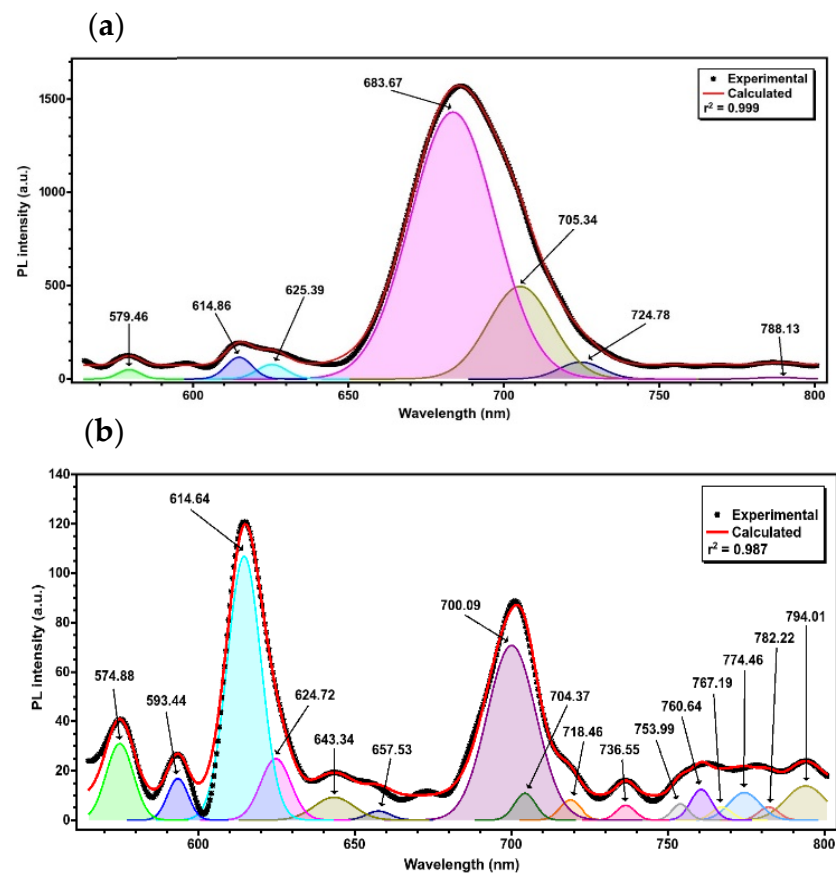


Figure 2. (a,b) PL spectra of MoS₂ and WS₂ on Si substrates, respectively.

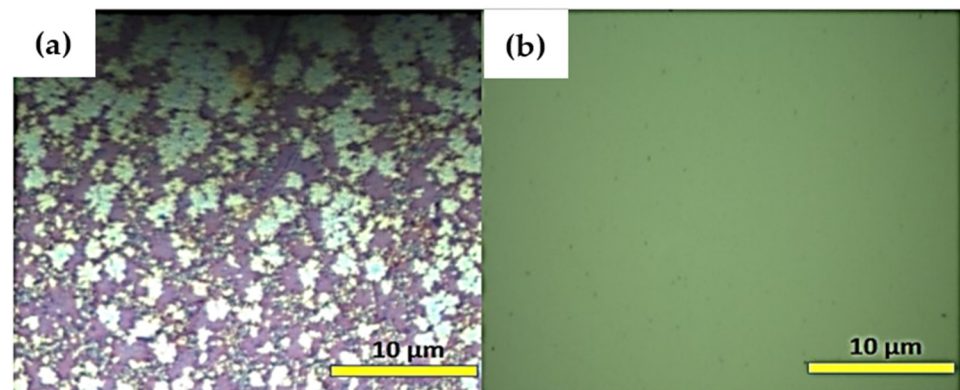


Figure 3. (a) MoS₂ and (b) WS₂ thin-film optical microscopy images.

The high-resolution FE-SEM images show quite a homogeneous distribution of a few nanometers that contain nanocrystals for both materials (Figure 4). However, the particles of MoS₂ are relatively smaller than those of WS₂. In both materials, particles are well interconnected to each other. Nevertheless, the WS₂ surface contains more cracks than MoS₂, which is important for surface gas adsorption and light-trapping applications [54].

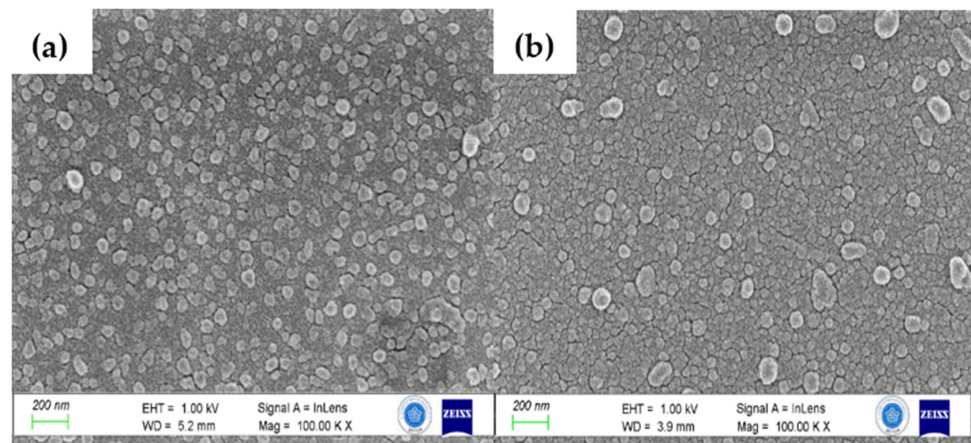


Figure 4. (a,b) FE-SEM morphology of MoS₂ and WS₂ thin films.

The topography of the prepared samples was measured by AFM using a noncontact mode of a $1 \times 1 \mu\text{m}$ area. Figure 5a,b show the 3D AFM topography and the horizontal line profile of MoS₂ and WS₂ samples, respectively. The roughness values of MoS₂ and WS₂ are 10.689 and 2.761 nm, respectively, as depicted in Table 1. The optical microscopy analysis also shows that MoS₂ has higher surface roughness than WS₂ film.

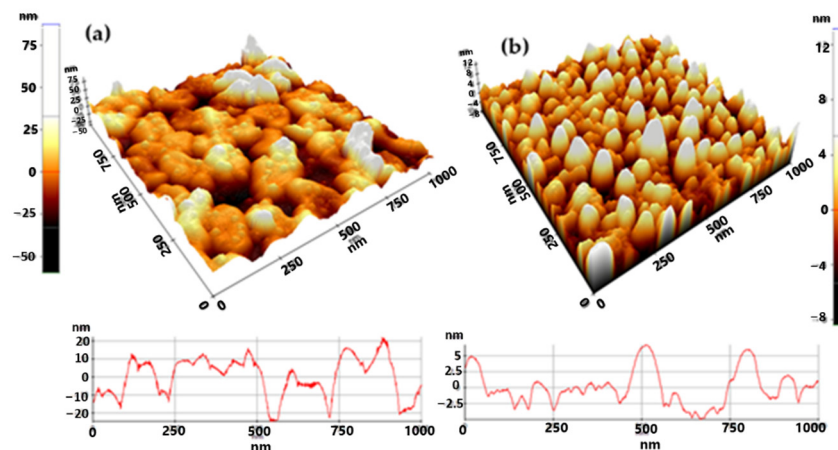


Figure 5. AFM topography and the horizontal line profile: (a,b) 3D topography images and corresponding line profile of MoS₂ and WS₂ samples, respectively.

Table 1. AFM roughness parameters of MoS₂ and WS₂ samples.

Sample	Region	Min (nm)	Max (nm)	Mid (nm)	R _q (nm)	R _a (nm)	R _z (nm)	R _{sk}	R _{ku}
MoS ₂	Line	−24.584	22.080	−1.252	46.664	10.689	9.200	45.329	0.439
WS ₂	Line	−4.964	6.682	0.859	11.646	2.761	2.099	11.374	−0.645

3.3. XPS and Oxidation States

The WS₂ and MoS₂ chemical states were examined through XPS survey analyses. The binding energies of S 2p, Mo 3d, C 1s, and O 1s are introduced by the characteristic peaks at 161 eV, 230 eV, 285 eV, and 532 eV, respectively [55], as shown in Figure 6a. The XPS survey analyses of WS₂ showed distinct signals of C, O, S, and W elements, as seen in Figure 6b. The W 4d_{3/2} spin-orbital splitting photoelectrons in the WS₂ nanostructures are reconsidering the W peak at 283.0 eV [56]. In addition, the W 4d_{3/2} peak binding energy is higher than the W atom, which confirms the presence of W with a valence of +4 [57].

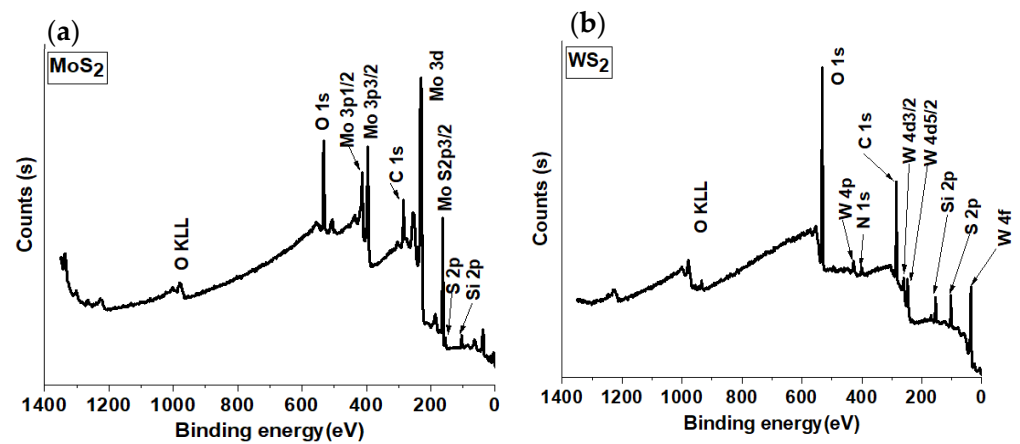


Figure 6. (a,b) General XPS survey spectrum distributions of both MoS₂ and WS₂ thin films.

3.4. Sheet Resistance and Hall Coefficient

Electrical characterization of the prepared MoS₂ and WS₂ thin films was carried out using a Hall-effect measurement system (Table 1). Table 2 displays the R_s (sheet resistance), R_{ho} (resistivity), V_H (Hall voltage), R_H (Hall coefficient), N_s/P_s (sheet carrier concentration), N/P (carrier concentration), and Mob (mobility). When V_H has a positive (negative) value, the majority of the sample's carriers are of the p (n) type. All measurements were performed with a 7210 G magnetic field and a temperature of 300 K. We observed an enhancement in the electrical mobility properties of the WS₂ compared to the MoS₂ thin film. The MoS₂ film shows an n-type and WS₂ is p-type semiconductor behavior [58]. Based on these investigations of Hall-effect measurements, it was observed that our devices are MoS₂ (n-type)/Si (p-type) and WS₂ (P-type)/Si (p-type) heterojunctions. The highest carrier concentration, as well as carrier mobility for p-p heterostructure, was higher than that of the p-n device, suggesting better performance for the WS₂/Si device.

Table 2. Room-temperature surface resistance and Hall-effect measurements for MoS₂ and WS₂ on a silicon substrate.

Sample	R_s (Ω/sq)	R_{ho} ($\Omega\text{-cm}$)	V_H (V)	R_H (m^3/C)	Type	N_s/P_s ($/cm^2$)	N/P ($/cm^3$)	Mobility (cm^2/V)
MoS ₂	1890	0.00284	−0.0129	−0.00000268	N	−3,500,000,000,000	−2,330,000,000,000,000,000	946
WS ₂	38,200	0.0573	0.00819	0.00000171	P	5,500,000,000,000	3,670,000,000,000,000,000	2980

3.5. Electric and Optoelectronic Characteristics

The current-voltage (I-V) electrical characteristics of MoS₂ and WS₂ were examined under air conditions in absence of light and 365 nm ultraviolet illuminations. The device size was $1 \times 1 \text{ cm}^2$, and we used silver paste for making the contacts with a width of 3 mm and a length of 1 cm. The vertical electron transfer (electrical and optoelectronic) multilayered MoS₂/Si and WS₂/Si heterostructures were investigated and active edge sites with high density [59] are shown in Figure 7. As mentioned above, a high resistance layer like SiO₂ [60], which increased the ideal structure vertical conductivity, is not presented in the currently optimized photodetector.

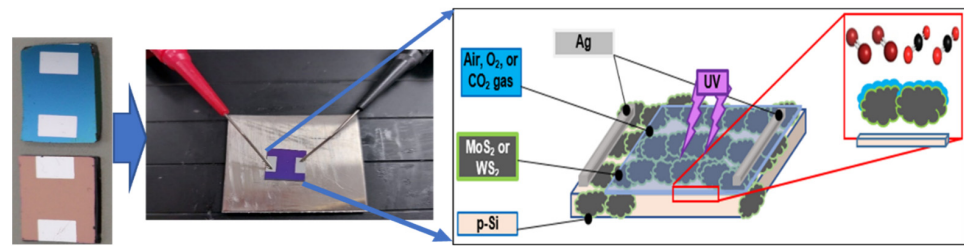


Figure 7. The MoS₂ and WS₂ photodetector under the illumination of UV light and the device's actual image as seen through the probe station. The measurements were carried out in the air, O₂, and CO₂ environments.

MoS₂: The idea of measuring the optoelectronic performance of devices under different gas stimuli, such as CO₂, has received much interest for many environmental and industrial applications. The behavior of optoelectronic photodetectors under a toxic gas environment such as CO₂ may predict the general performance of devices. Figure 8 shows the I-V curve of MoS₂ in dark and UV conditions of 365 nm under air and CO₂ gas stimuli. Under dark and illumination conditions, nonlinear I-V curves were observed, showing the generation of an excellent double-Schottky contact between the silver (Ag) electrode and film surfaces, as predicted before [61]. The observed photocurrent is small compared to the dark current in the air. Under CO₂ gas flow, the photocurrent is lower than the one under air in both positive and negative parts. This result shows the n-type behavior of MoS₂ under CO₂. CO₂ gas can capture the electrons from the conduction band of the n-type MoS₂ surface, which consequently can decrease the current. Since CO₂ does not absorb light at 365 nm, the reduction in photocurrent is related to its oxidizing properties that act on the MoS₂ surface. Similar behavior has been predicted before for different n-type semiconductor materials [42,43]. Moreover, by increasing the CO₂ gas flow from 50 to 150 sccm, a further but less pronounced photocurrent decrease is observed, supporting the effect of oxidation.

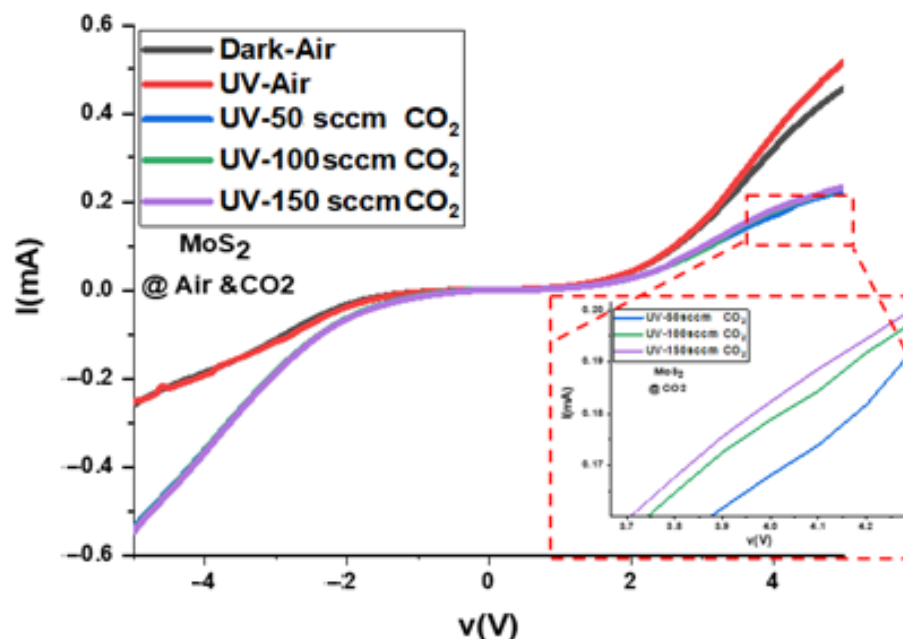


Figure 8. I-V characteristic of MoS₂ in the absence of light and UV illumination conditions under air and CO₂.

To check the behavior of the MoS₂ photodetector with time, we measured the change in the photocurrent in the air under dark and light illumination conditions, as shown in Figure 9a. The measurements are carried out at different bias voltages from 0 to 5 V. The MoS₂ in air did not show a good response at zero bias, but the response started to appear

from 0.5 V. With increased applied bias, the sensor performance becomes dominated and more stable and produces higher photocurrent. Figure 9b shows the on–off time-resolved photoresponse of MoS₂ thin film under a different bias voltage of 0–5 V. The measurements were recorded every 30 s and started with dark mode followed by the UV-on illumination mode. The dynamic curve of the MoS₂ at zero bias did not show a good signal, confirming that it is not a self-bias photodetector. However, with a small bias of 0.5 V, a clear signal gets released. We see that at higher applied biases, the device is working more efficiently, as expected.

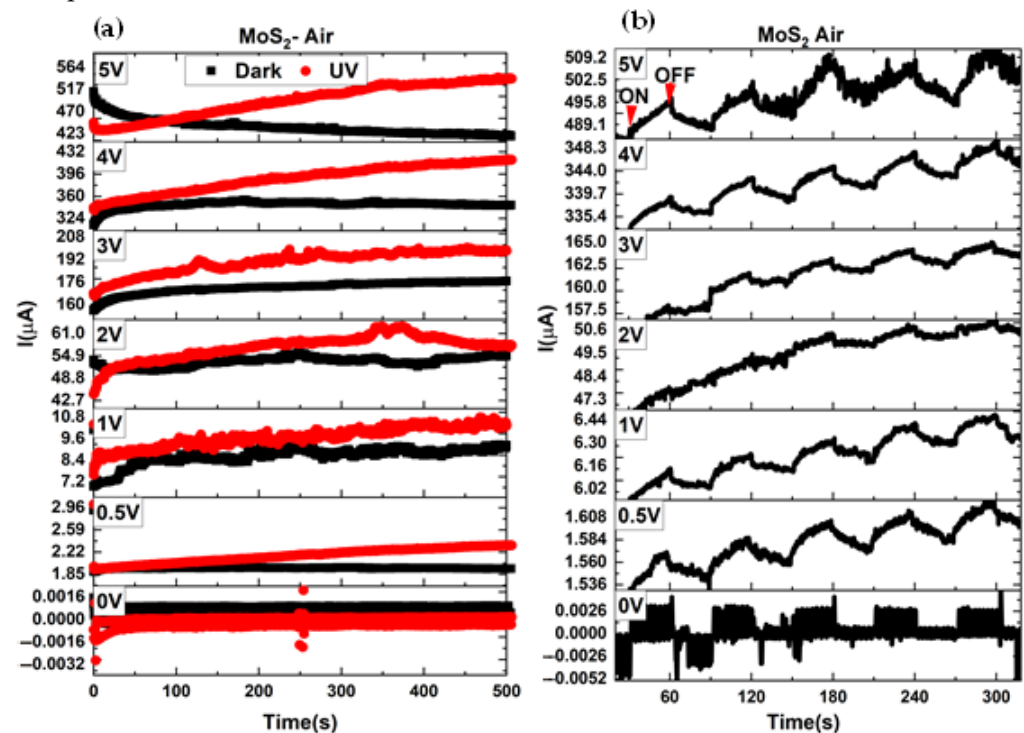


Figure 9. (a) Photocurrent behavior with time of MoS₂ under dark and UV illumination conditions in air, and (b) the on–off time-resolved photoresponse of MoS₂ thin film under bias voltages of 0–5 V.

To check the photocurrent time and the on–off behavior of the MoS₂ photodetector in air and CO₂, we chose a bias of 5 V. Figure 10a,b show the photocurrent behavior with time and on–off time-resolved photoresponse of MoS₂ thin film under the absence of light and UV illumination conditions in both air and 50 sccm CO₂ environments at a bias voltage of 5 V. The behavior of the photocurrent in both cases (air and CO₂) is more or less the same. Therefore, in the case of CO₂, we see that the dark current is decaying with time but the photocurrent is increasing, similar to the case of air. However, the decreasing and increasing rate of the current for the case of CO₂ stimuli is less than in the case of air, confirming the better stability of the MoS₂ photodetector in CO₂ than in an air environment. The position of the CO₂ curve is lower than that of the air, due to the capturing mechanism of the CO₂ of electrons and subsequently increasing the resistance. On the other hand, for the on–off curve in Figure 10b, the MoS₂ photodetector in CO₂ long-term stability with time is better than in the case of air. In both cases, the response and recovery time are relatively long.

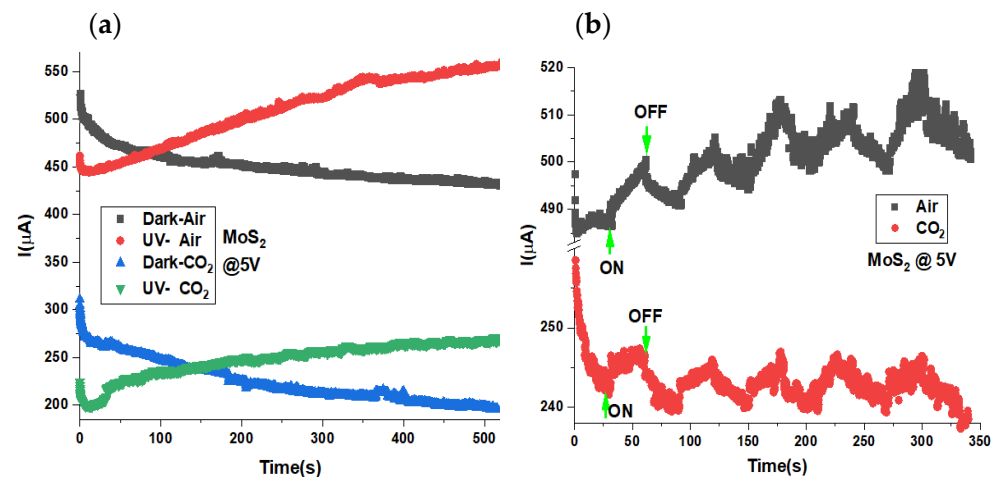


Figure 10. (a,b) Photocurrent behavior with time and on–off time-resolved photoresponse of MoS₂ thin film under dark and UV illumination conditions in both air and 50 sccm CO₂ environments at a bias voltage of 5 V.

On the other hand, for WS₂, we observed a better response than MoS₂ thin film. We measured the electrical IV properties of WS₂ thin film under dark and UV illuminations in air, O₂, and CO₂ environments, as in Figure 11. The IV curve in air is illustrated in Figure 11a. We observed a better response under light illumination in both positive and negative parts than in the case of MoS₂ thin film. However, for the IV of MoS₂ above, only a small improvement in the positive current was shown, but there were no changes in the negative section. This indicated that WS₂ is more interesting for optoelectronic applications, so we tested WS₂ film under O₂ and CO₂ environments. In the case of 100 sccm O₂ stimuli, its photocurrent is decreasing for both dark and UV cases, as represented in Figure 11b. This shows that the Fermi level's position has a substantial effect on O₂ and CO₂ molecule adsorption and desorption at the surface. Charge transfer is expected to attract electrons from the p-type WS₂ layer because CO₂ is an electronegative molecule [62].

Normally, O₂ and CO₂ are oxidizing gases due to their high affinity for electrons and high electronegativity. However, in the case of CO₂ molecules, the electronegativity is stronger than in the O₂ case. We observed an increase in the photocurrent under the CO₂ environment in Figure 11c. The photocurrent is increased with increasing the CO₂ concentrations from 50 to 200 sccm. The p-type semiconductor behavior of WS₂ under CO₂ adsorption increases the total current as observed here in Figure 11. To check the WS₂ film stability under air, we measured the photocurrent behavior as a function of time of WS₂ thin film under the dark condition in the air at a different bias voltage of 0, 0.5, 1, and 2 V, as demonstrated in Figure 12a. In the case of WS₂, we found that the film became more stable at low bias voltage, in contrast to the case of MoS₂, so we did not test the WS₂ films at higher bias voltage. By increasing the bias voltage, the current was increased. However, by applying 2 V, the current reached higher values. Consequently, the on–off behavior of WS₂ thin film was tested under the same applied biases of 0, 0.5, 1, and 2 V and is depicted in Figure 12b. At 0 V bias, for the dark current in the air, almost no current is observed with some signal noises. But under O₂ stimuli, we observed a negative current behavior as in Figure 12b, indicating that WS₂ can work as a negative photoresponse optical detector under low biases [40]. However, at 0.5, 1, and 2 V bias, the current becomes positive for under air and O₂ environments. At 0.5 and 1 V, there were almost no changes in the current under air and O₂ gas environments. The best current response was observed at 2 V for both air and O₂ environments with the same behavior, as expected (Figure 12b).

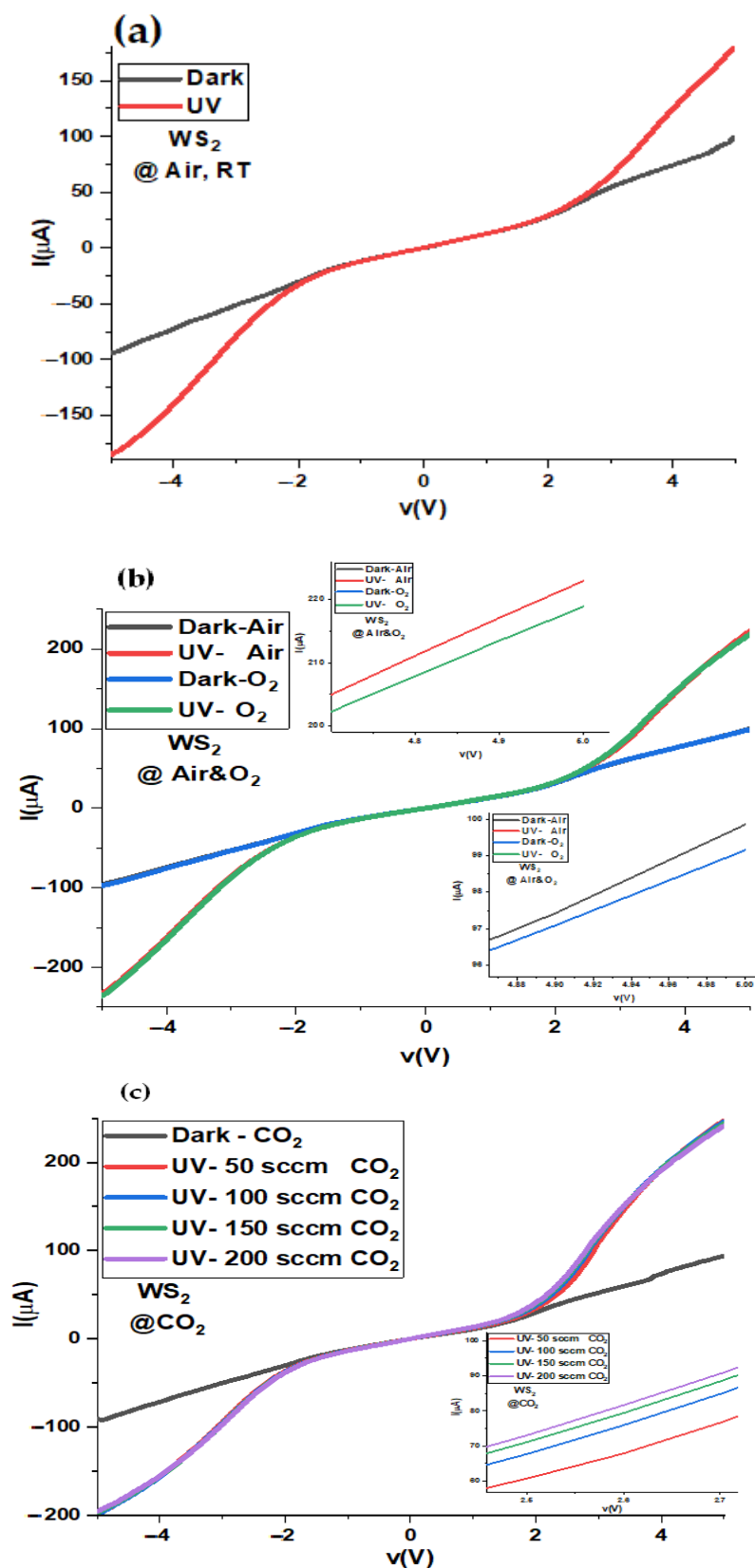


Figure 11. Characteristic I-V curve of WS_2 under dark and UV illumination conditions under (a) air environment, (b) O_2 environment and (c) CO_2 environment.

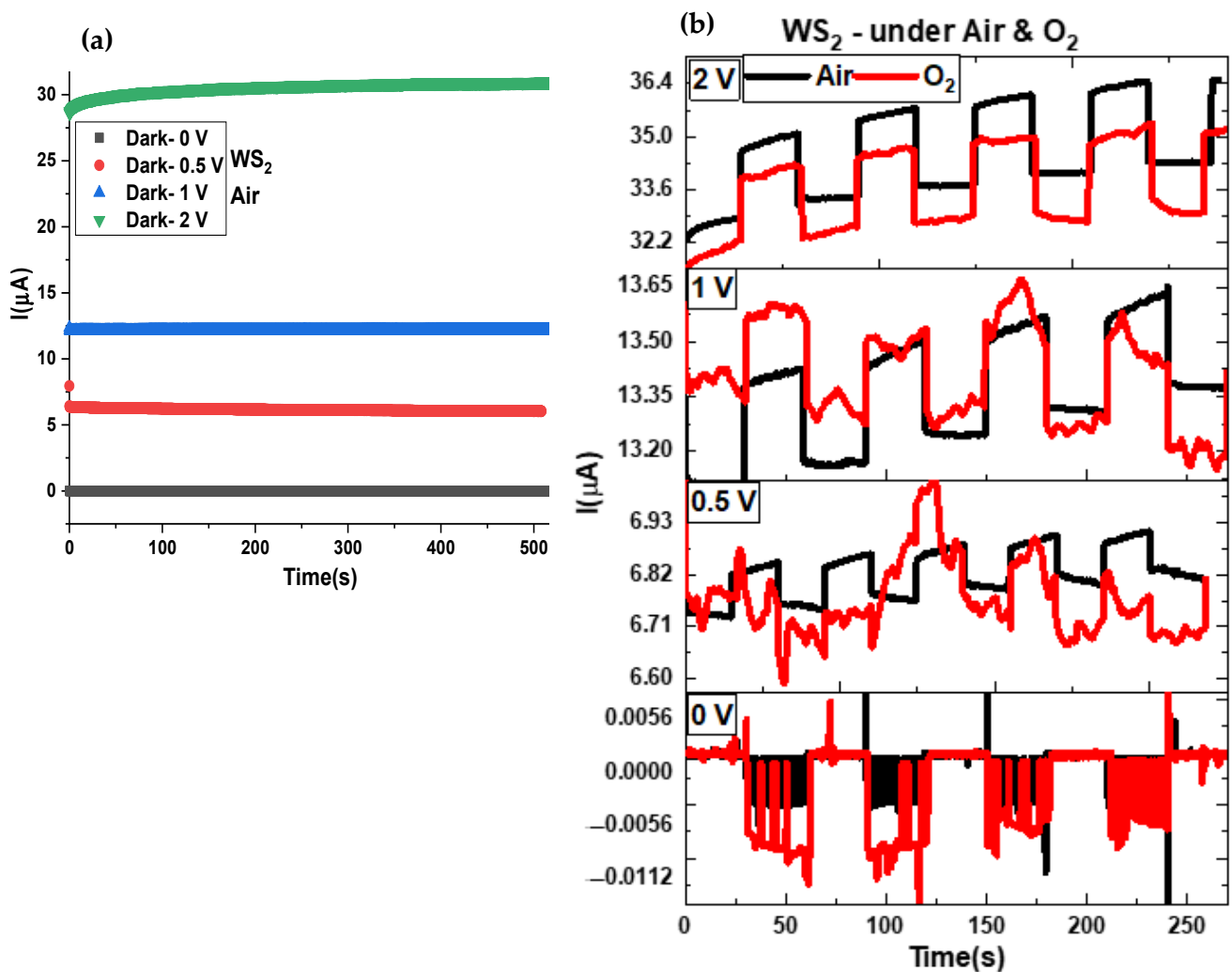


Figure 12. (a) Photocurrent behavior with the time of WS_2 thin film under a dark condition in the air at a different bias voltage of 0, 0.5, 1, and 2 V. (b) The on–off dynamics of the current with a time of WS_2 thin film in air and 50 sccm O_2 environments under a different bias voltage of 0–2 V.

By these means, we measured the photocurrent of WS_2 at 2 V under air and CO_2 . Figure 13a show the photocurrent behavior with a time of WS_2 thin film under dark and UV conditions in CO_2 at a bias voltage of 2 V. We see that the general behavior is positive photoresponse. The demonstrated results show that WS_2 film presented long-term stability in CO_2 and also in the air with time. Figure 13b shows the on–off photoresponse dynamics of WS_2 thin film in air, 50 sccm O_2 , and 50 sccm CO_2 environments under a bias voltage of 2 V. The photocurrent of WS_2 thin film is largely enhanced by introducing CO_2 gas under UV illumination. In contrast, for the air and O_2 environment, we do not see a large enhancement in the photocurrent. The on–off curve shows high stability during many pulses. Under the same conditions, the WS_2 introduced a higher sensitivity to environmental gases including CO_2 and O_2 than MoS_2 thin film. In addition, we found that the high photocurrent is shown under the CO_2 stimuli for WS_2 under various gas conditions.

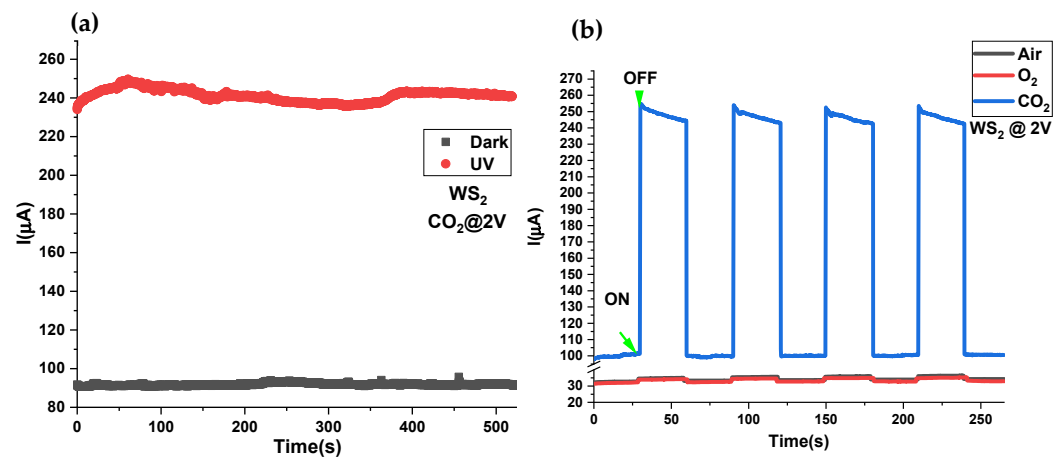


Figure 13. (a) Photocurrent behavior with time of WS_2 thin film under dark and UV conditions in CO_2 at a bias voltage of 2 V. (b) The on–off dynamics of the photoresponse with a time of WS_2 thin film in air, 50 sccm O_2 , and 50 sccm CO_2 environments under a bias voltage of 2 V.

3.6. Transient Response

The MoS_2 and WS_2 thin-film response and recovery time under UV illumination of 365 nm are depicted in Figure 14. The MoS_2 and WS_2 on–off behavior gives us a sense of the rise and fall with time under dark and illumination conditions. The response/rise time was calculated when the source of light opened, and when the light was turned off, the recovery/decay time was measured. The MoS_2 thin film has a longer recovery time and faster response time in an air environment, as in Figure 14a. However, under CO_2 stimuli, a longer response/recovery time is noted. The longer response time may refer to the CO_2 gas adsorption on MoS_2 , which is faster than the desorption kinetics. The observed response/recovery time of MoS_2 is in seconds, which limits the application of the MoS_2 photodetector. However, for the WS_2 thin film, a faster response is observed, as in Figure 14b. Generally, the WS_2 thin film introduced a shorter response time than the recovery time. In addition, shorter response and recovery times are observed for the CO_2 case compared with air and O_2 stimuli. The CO_2 adsorption/desorption kinetics on WS_2 are faster than in the air and O_2 gas cases. The adsorption energy and diffusion coefficient of O_2 were the lowest [63].

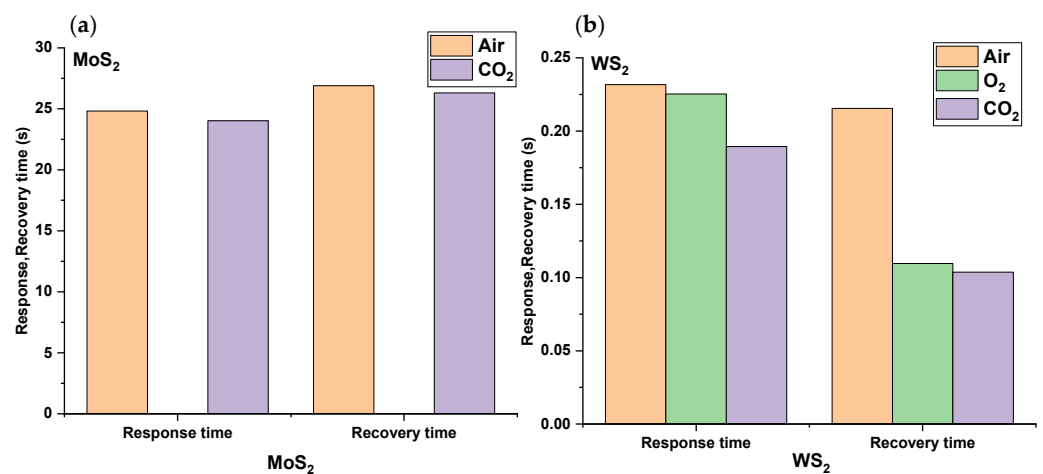


Figure 14. Shows the response and therecovery times for (a) MoS_2 and (b) WS_2 thin films under gas stimuli.

3.7. Photocurrent Gain (P_g), Photoresponsivity (R_λ), External Quantum Efficiency (EQE) and Detectivity (D^*)

Some other parameters may contribute to the general performance of the photodetector sensor, such as photocurrent gain (P_g), photoresponsivity (R_λ), external quantum efficiency (EQE), and detectivity (D^*). $I_{ph} = I_{Light} - I_{Dark}$ gives the induced photocurrent I_{ph} , where I_{ph} increases as the applied voltage and light power increase [64]. Here, the light intensity is maintained at a consistent level and excitation wavelength of 365 nm. Photocurrent gain (P_g), responsivity (R_λ), and external quantum efficiency can be calculated as reported before [23,24,65,66]. The detectable signal is another significant figure of merit for a photodetector referred by the specific detectivity [67]. The parameters of I_{ph} , P_g , R_λ , EQE, and D^* for MoS₂ and WS₂ thin films are reported in Table 3. It seems that the general performance of MoS₂ is weaker than WS₂ thin film. The I_{ph} of MoS₂ is decreased by introducing CO₂ as explained in Figure 8. Consequently, all the other parameters will get affected in a similar way. The EQE of MoS₂ thin film under air is higher than that in CO₂.

Table 3. The photocurrent (I_{ph}), photocurrent gain (P_g), photoresponsivity (R_λ), external quantum efficiency (EQE), and detectivity (D^*) of MoS₂ and WS₂ samples.

Sample	Gas	Photocurrent (A)	Photocurrent Gain (a.u.)	Responsivity ($\mu\text{A/mW}$)	EQE	D^*
MoS ₂	Air	0.0000131	0.0270	6.5745	13,900,000	372.05
	CO ₂	0.00000635	0.0265	3.1765	6,740,000	256.34
WS ₂	Air	0.00000207	0.0631	1.035	2,200,000	225.76
	CO ₂	0.000153	1.51	76.50	162,000,000	9509.10
	O ₂	0.00000183	0.0568	0.915	1,940,000	201.34

The photocurrent and photocurrent gain of MoS₂ and WS₂ under air and CO₂ are represented in Figure 15. For WS₂ film, a clear enhancement in both photocurrent and photocurrent gain is observed under CO₂ stimuli. In the case of WS₂ thin film, we introduced a p-type semiconductor with a large carrier concentration value of $5,500,000,000,000\text{ cm}^{-2}$; consequently, a high photocurrent is observed in the air. We observed a large enhancement in the EQE in the air of 2,200,000 compared with CO₂ of 162,000,000, due to the fact that CO₂ is an oxidizing agent interacting with p-type semiconductor materials, which can improve the electron concentrations and increase the conductivity of the film, as in Figure 15b [68]. Under O₂ stimuli, we observed a lower responsivity of 0.915 $\mu\text{A/mW}$. On the other hand, for the MoS₂ thin film, we have an n-type semiconductor that is interacting with oxidizing CO₂ gas, which will increase the film resistance and consequently decrease the photocurrent, as in Figure 15a.

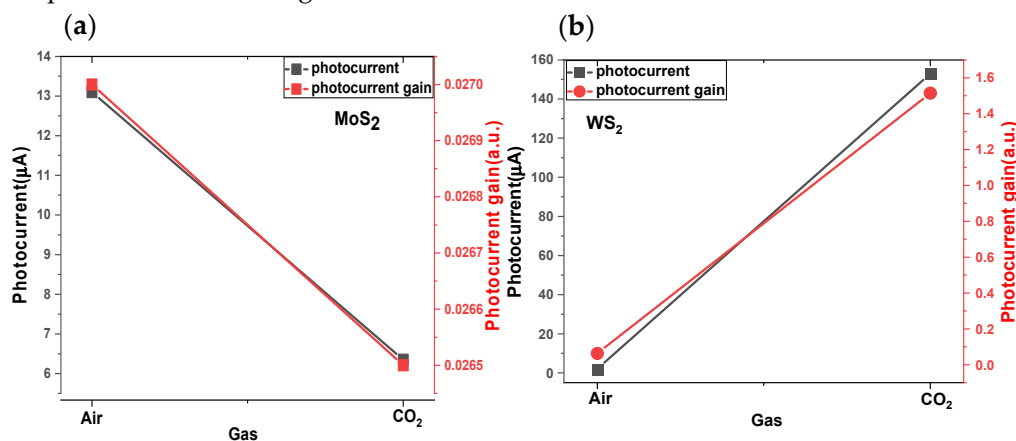


Figure 15. (a,b) Photocurrent and photocurrent gain of MoS₂ and WS₂ thin film under gas stimuli.

4. Conclusions

A 2D transition metal dichalcogenide heterojunctions of MoS₂ and WS₂ on silicon substrates for optoelectronic applications have been introduced. Using commercial chemical and physical vapor deposition techniques, we combined them for large-scale photodetector applications and beyond. For the first time, we exposed CO₂ and O₂ gases through a designed chamber to test their effects on the UV photodetector applications. The semiconducting behavior of MoS₂ and WS₂ thin films are n- and p-type with sheet carrier concentrations of 3,500,000,000,000 and 5,500,000,000,000 cm⁻². The WS₂ thin film showed higher carrier mobility of 2980 cm²/V compared to 946 cm²/V of MoS₂ film. WS₂ showed a fast response under UV illumination than MoS₂ under air, CO₂, and O₂ environments. The calculated detectivity of WS₂ showed higher values compared to the air and O₂ adsorbed gases. We also observed that the EQE of WS₂ under CO₂ is 162,000,000 compared with 6,740,000 for the case of MoS₂ thin film. Our findings provide high motivation for using MoS₂ and WS₂ thin films for space and industrial applications filled with environmental gases.zzzz

Author Contributions: Conceptualization, M.A.B. and S.E.Z.; methodology, M.A.B. and S.E.Z.; validation, M.A.B., S.E.Z., Y.R.E., M.Y., N.A., M.T., G.F.A. and M.S.; formal analysis, M.A.B., S.E.Z., Y.R.E., M.S. and M.Y.; investigation, M.A.B., S.E.Z., M.Y., M.T., N.A., M.S. and Y.R.E.; resources, M.A.B., Ş.A., S.E.Z., M.Y., Y.R.E., N.A., G.F.A. and M.S.; data curation, M.A.B., Ş.A., S.E.Z., N.A. and M.S.; writing—original draft preparation, M.A.B., S.E.Z. and M.Y.; writing—review and editing, M.A.B., S.E.Z., Y.R.E., M.Y., M.T., N.A., G.F.A. and M.S.; visualization, M.A.B., Ş.A., N.A., G.F.A. and M.S.; supervision, M.A.B., Y.R.E. and M.Y.; project administration, M.A.B., Ş.A., N.A. and M.S.; funding acquisition, M.A.B., N.A. and M.S. All authors have read and agreed to the published version of the manuscript.

Funding: Princess Nourah bint Abdulrahman University Researchers Supporting Project (PNURS-P2022R291), Princess Nourah bint Abdulrahman University, Riyadh, Saudi Arabia.

Data Availability Statement: Not applicable.

Acknowledgments: The authors express their gratitude to Princess Nourah bint Abdulrahman University Researchers Supporting Project (PNURSP2022R291), Princess Nourah bint Abdulrahman University, Riyadh, Saudi Arabia. The first and the second authors would like to thank the Abdus Salam International Centre for Theoretical Physics (ICTP) Trieste TS, Italy for the building discussions, support, and tremendous multidisciplinary talks and events.

Conflicts of Interest: The authors declare no conflict of interest.

References

- Gonzalez-Cuevas, J.A.; Refaat, T.F.; Abedin, M.N.; Elsayed-Ali, H.E. Modeling of the Temperature-Dependent Spectral Response of In_(1-x)Ga_xSb Infrared Photodetectors. *Opt. Eng.* **2006**, *45*, 44001.
- Basyooni, M.A.; Shaban, M.; El Sayed, A.M. Enhanced Gas Sensing Properties of Spin-coated Na-doped ZnO Nanostructured Films. *Sci. Rep.* **2017**, *7*, 41716. [[CrossRef](#)] [[PubMed](#)]
- Zaki, S.E.; Basyooni, M.A. Ultra-sensitive gas sensor based fano resonance modes in periodic and fibonacci quasi-periodic Pt/PtS₂ structures. *Sci. Rep.* **2022**, *12*, 9759. [[CrossRef](#)] [[PubMed](#)]
- Zaki, S.E.; Basyooni, M.A.; Shaban, M.; Rabia, M.; Eker, Y.R.; Attia, G.F.; Yilmaz, M.; Ahmed, A.M. Role of oxygen vacancies in vanadium oxide and oxygen functional groups in graphene oxide for room temperature CO₂ gas sensors. *Sens. Actuators A Phys.* **2019**, *294*, 17–24. [[CrossRef](#)]
- Owen, T. *The Composition and Early History of the Atmosphere of Mars*; Mars Publication: Hong Kong, China, 2018; pp. 818–834.
- Elías, A.L.; Perea-López, N.; Castro-Beltrán, A.; Berkdemir, A.; Lv, R.; Feng, S.; Long, A.D.; Hayashi, T.; Kim, Y.A.; Endo, M.; et al. Controlled synthesis and transfer of large-area WS₂ sheets: From single layer to few layers. *ACS Nano* **2013**, *7*, 5235–5242. [[CrossRef](#)]
- Huo, N.; Yang, S.; Wei, Z.; Li, S.S.; Xia, J.B.; Li, J. Photoresponsive and Gas Sensing Field-Effect Transistors based on Multilayer WS₂ Nanoflakes. *Sci. Rep.* **2014**, *4*, 5209. [[CrossRef](#)] [[PubMed](#)]
- Georgiou, T.; Jalil, R.; Belle, B.D.; Britnell, L.; Gorbachev, R.V.; Morozov, S.V.; Kim, Y.J.; Gholinia, A.; Haigh, S.J.; Makarovskiy, O.; et al. Vertical field-effect transistor based on graphene-WS₂ heterostructures for flexible and transparent electronics. *Nat. Nanotechnol.* **2013**, *8*, 100–103. [[CrossRef](#)]
- Bernardi, M.; Palummo, M.; Grossman, J.C. Extraordinary sunlight absorption and one nanometer thick photovoltaics using two-dimensional monolayer materials. *Nano Lett.* **2013**, *13*, 3664–3670. [[CrossRef](#)]

10. Park, J.; Kim, M.S.; Cha, E.; Kim, J.; Choi, W. Synthesis of uniform single layer WS₂ for tunable photoluminescence. *Sci. Rep.* **2017**, *7*, 16121. [[CrossRef](#)]
11. Das, U.; Bhattacharjee, S.; Mahato, B.; Prajapat, M.; Sarkar, P.; Roy, A. Uniform, large-scale growth of WS₂ nanodomains via CVD technique for stable non-volatile RRAM application. *Mater. Sci. Semicond. Process.* **2020**, *107*, 104837. [[CrossRef](#)]
12. Lin, Y.; Adilbekova, B.; Firdaus, Y.; Yengel, E.; Faber, H.; Sajjad, M.; Zheng, X.; Yarali, E.; Seitkhan, A.; Bakr, O.M.; et al. 17% Efficient Organic Solar Cells Based on Liquid Exfoliated WS₂ as a Replacement for PEDOT:PSS. *Adv. Mater.* **2019**, *31*, 1902965. [[CrossRef](#)]
13. Sharma, D.; Motayed, A.; Shah, P.B.; Amani, M.; Georgieva, M.; Glen Birdwell, A.; Dubey, M.; Li, Q.; Davydov, A. V Transfer characteristics and low-frequency noise in single- and multi-layer MoS₂ field-effect transistors. *Appl. Phys. Lett.* **2015**, *107*, 162102. [[CrossRef](#)]
14. Nicolosi, V.; Chhowalla, M.; Kanatzidis, M.G.; Strano, M.S.; Coleman, J.N. Liquid exfoliation of layered materials. *Science* **2013**, *340*, 1226419. [[CrossRef](#)]
15. Coleman, J.N. ChemInform Abstract: Two-Dimensional Nanosheets Produced by Liquid Exfoliation of Layered Materials. *ChemInform* **2011**, *42*, 568–571. [[CrossRef](#)]
16. Yu, X.; Prévot, M.S.; Sivula, K. Multiflake thin film electronic devices of solution processed 2D MoS₂ enabled by sonopolymer assisted exfoliation and surface modification. *Chem. Mater.* **2014**, *26*, 5892–5899. [[CrossRef](#)]
17. Paton, K.R.; Varrla, E.; Backes, C.; Smith, R.J.; Khan, U.; O'Neill, A.; Boland, C.; Lotya, M.; Istrate, O.M.; King, P.; et al. Scalable production of large quantities of defect-free few-layer graphene by shear exfoliation in liquids. *Nat. Mater.* **2014**, *13*, 624–630. [[CrossRef](#)]
18. Varrla, E.; Backes, C.; Paton, K.R.; Harvey, A.; Gholamvand, Z.; McCauley, J.; Coleman, J.N. Large-scale production of size-controlled MoS₂ nanosheets by shear exfoliation. *Chem. Mater.* **2015**, *27*, 1129–1139. [[CrossRef](#)]
19. Knirsch, K.C.; Berner, N.C.; Nerl, H.C.; Cucinotta, C.S.; Gholamvand, Z.; McEvoy, N.; Wang, Z.; Abramovic, I.; Vecera, P.; Halik, M.; et al. Basal-Plane Functionalization of Chemically Exfoliated Molybdenum Disulfide by Diazonium Salts. *ACS Nano* **2015**, *9*, 6018–6030. [[CrossRef](#)] [[PubMed](#)]
20. Eda, G.; Yamaguchi, H.; Voiry, D.; Fujita, T.; Chen, M.; Chhowalla, M. Photoluminescence from chemically exfoliated MoS₂. *Nano Lett.* **2011**, *11*, 5111–5116. [[CrossRef](#)] [[PubMed](#)]
21. Yang, X.Y. *Photoenergy and Thin Film Materials*; John Wiley & Sons: Hoboken, NJ, USA, 2019.
22. Giannazzo, F.; Lara Avila, S.; Eriksson, J.; Sonde, S. Integration of 2D Materials for Electronics Applications. *Crystals* **2019**, *7*, 162.
23. Ali, M.; Mohamed, B. VO₂ Ince Film İçeren İki Boyutlu Ve Çok Katmanlı Yapılardaki Arayüzey Gerilmelerinin Termokromik Ve Fotodetektör Performanslara Etkisi. Ph.D. Thesis, Necmettin Erbakan University, Konya, Turkey, 2020.
24. Basyooni, M.A.; Zaki, S.E.; Shaban, M.; Eker, Y.R.; Yilmaz, M. Efficient MoWO₃/VO₂/MoS₂/Si UV Schottky photodetectors; MoS₂ optimization and monoclinic VO₂ surface modifications. *Sci. Rep.* **2020**, *10*, 15926. [[CrossRef](#)] [[PubMed](#)]
25. Yu, J.; Li, J.; Zhang, W.; Chang, H. Synthesis of high quality two-dimensional materials via chemical vapor deposition. *Chem. Sci.* **2015**, *6*, 6705–6716. [[CrossRef](#)] [[PubMed](#)]
26. Cai, Z.; Liu, B.; Zou, X.; Cheng, H.M. Chemical Vapor Deposition Growth and Applications of Two-Dimensional Materials and Their Heterostructures. *Chem. Rev.* **2018**, *118*, 6091–6133. [[CrossRef](#)] [[PubMed](#)]
27. Wang, H.; Yu, L.; Lee, Y.H.; Fang, W.; Hsu, A.; Herring, P.; Chin, M.; Dubey, M.; Li, L.J.; Kong, J.; et al. Large-scale 2D electronics based on single-layer MoS₂ grown by chemical vapor deposition. In Proceedings of the Technical Digest—International Electron Devices Meeting, IEDM, San Francisco, CA, USA, 10–13 December 2012.
28. Browning, R.; Padigi, P.; Solanki, R.; Twest, D.J.; Schuele, P.; Evans, D. Atomic layer deposition of MoS₂ thin films. *Mater. Res. Express* **2015**, *2*, 025006. [[CrossRef](#)]
29. Loh, T.A.J.; Chua, D.H.C. Growth mechanism of pulsed laser fabricated few-layer MoS₂ on metal substrates. *ACS Appl. Mater. Interfaces* **2014**, *6*, 15966–15971. [[CrossRef](#)] [[PubMed](#)]
30. Serrao, C.R.; Diamond, A.M.; Hsu, S.L.; You, L.; Gadgil, S.; Clarkson, J.; Carraro, C.; Maboudian, R.; Hu, C.; Salahuddin, S. Highly crystalline MoS₂ thin films grown by pulsed laser deposition. *Appl. Phys. Lett.* **2015**, *106*, 052101. [[CrossRef](#)]
31. Basyooni, M.A.; Al-Dossari, M.; Zaki, S.E.; Eker, Y.R.; Yilmaz, M.; Shaban, M. Tuning the Metal-Insulator Transition Properties of VO₂ Thin Films with the Synergetic Combination of Oxygen Vacancies, Strain Engineering, and Tungsten Doping. *Nanomaterials* **2022**, *12*, 1470. [[CrossRef](#)] [[PubMed](#)]
32. Ma, X.; Shi, M. Thermal evaporation deposition of few-layer MoS₂ films. *Nano-Micro Lett.* **2013**, *5*, 135–139. [[CrossRef](#)]
33. Wu, S.; Huang, C.; Aivazian, G.; Ross, J.S.; Cobden, D.H.; Xu, X. Vapor-solid growth of high optical quality MoS₂ monolayers with near-unity valley polarization. *ACS Nano* **2013**, *7*, 2768–2772. [[CrossRef](#)] [[PubMed](#)]
34. Pacley, S.; Hu, J.; Jespersen, M.; Hilton, A.; Waite, A.; Brausch, J.; Beck-Millerton, E.; Voevodin, A.A. Impact of reduced graphene oxide on MoS₂ grown by sulfurization of sputtered MoO₃ and Mo precursor films. *J. Vac. Sci. Technol. A Vac. Surf. Film.* **2016**, *34*, 041505. [[CrossRef](#)]
35. Hussain, S.; Shehzad, M.A.; Vikraman, D.; Khan, M.F.; Singh, J.; Choi, D.C.; Seo, Y.; Eom, J.; Lee, W.G.; Jung, J. Synthesis and characterization of large-area and continuous MoS₂ atomic layers by RF magnetron sputtering. *Nanoscale* **2016**, *8*, 4340–4347. [[CrossRef](#)] [[PubMed](#)]
36. Matsuura, K.; Ohashi, T.; Muneta, I.; Ishihara, S.; Kakushima, K.; Tsutsui, K.; Ogura, A.; Wakabayashi, H. Low-Carrier-Density Sputtered MoS₂ Film by Vapor-Phase Sulfurization. *J. Electron. Mater.* **2018**, *47*, 3497–3501. [[CrossRef](#)]

37. Furchi, M.M.; Polyushkin, D.K.; Pospischil, A.; Mueller, T. Mechanisms of photoconductivity in atomically thin MoS₂. *Nano Lett.* **2014**, *14*, 6165–6170. [CrossRef] [PubMed]
38. Han, P.; Adler, E.R.; Liu, Y.; St Marie, L.; El Fatimy, A.; Melis, S.; van Keuren, E.; Barbara, P. Ambient effects on photogating in MoS₂ photodetectors. *Nanotechnology* **2019**, *30*, 284004. [CrossRef]
39. Pospischil, A.; Mueller, T. Optoelectronic devices based on atomically thin transition metal dichalcogenides. *Appl. Sci.* **2016**, *6*, 78. [CrossRef]
40. Klement, P.; Steinke, C.; Chatterjee, S.; Wehling, T.O.; Eickhoff, M. Effects of the Fermi level energy on the adsorption of O₂ to monolayer MoS₂. *2D Mater.* **2018**, *5*, 045025. [CrossRef]
41. Kumar, R.; Zheng, W.; Liu, X.; Zhang, J.; Kumar, M. MoS₂-Based Nanomaterials for Room-Temperature Gas Sensors. *Adv. Mater. Technol.* **2020**, *5*, 1901062. [CrossRef]
42. Khan, M.A.; Kumawat, K.L.; Nanda, K.K.; Krupanidhi, S.B. Reduced graphene oxide-based broad band photodetector and temperature sensor: Effect of gas adsorption on optoelectrical properties. *J. Nanoparticle Res.* **2018**, *20*, 293. [CrossRef]
43. Yan, H.J.; Xu, B.; Shi, S.Q.; Ouyang, C.Y. First-principles study of the oxygen adsorption and dissociation on graphene and nitrogen doped graphene for Li-air batteries. *J. Appl. Phys.* **2012**, *112*, 112602. [CrossRef]
44. Guo, R.; Han, D.; Chen, W.; Dai, L.; Ji, K.; Xiong, Q.; Li, S.; Reb, L.K.; Scheel, M.A.; Pratap, S.; et al. Degradation mechanisms of perovskite solar cells under vacuum and one atmosphere of nitrogen. *Nat. Energy* **2021**, *6*, 977–986. [CrossRef]
45. Karataş, A.; Yılmaz, M. Molybdenum disulfide thin films fabrication from multi-phase molybdenum oxide using magnetron sputtering and CVD systems together. *Superlattices Microstruct.* **2020**, *143*, 106555. [CrossRef]
46. Basyooni, M.A.; Eker, Y.R.; Yılmaz, M. Van-der Waals 2-Dimensional Nanostructured Molybdenum and Tungsten Disulfide-Si Heterostructure Photodetector under Different Environment Stimuli for High Yield Optoelectronics. *Mühendislik Bilimleri* **2020**, *2*.
47. Shanmugam, M.; Durcan, C.A.; Yu, B. Layered semiconductor molybdenum disulfide nanomembrane based Schottky-barrier solar cells. *Nanoscale* **2012**, *4*, 7399–7405. [CrossRef] [PubMed]
48. Basyooni, M.A.; Zaki, S.E.; Tihiti, M.; Eker, Y.R.; Ateş, Ş. Photonic bandgap engineering in (VO₂)_n/(WSe₂)_n photonic superlattice for versatile near- and mid-infrared phase transition applications. *J. Phys. Condens. Matter* **2022**, *34*, 325901. [CrossRef] [PubMed]
49. Splendiani, A.; Sun, L.; Zhang, Y.; Li, T.; Kim, J.; Chim, C.Y.; Galli, G.; Wang, F. Emerging photoluminescence in monolayer MoS₂. *Nano Lett.* **2010**, *10*, 1271–1275. [CrossRef] [PubMed]
50. Zhu, Z.Y.; Cheng, Y.C.; Schwingenschlögl, U. Giant spin-orbit-induced spin splitting in two-dimensional transition-metal dichalcogenide semiconductors. *Phys. Rev. B Condens. Matter Mater. Phys.* **2011**, *84*, 153402. [CrossRef]
51. Zhao, W.; Ghorannevis, Z.; Chu, L.; Toh, M.; Kloc, C.; Tan, P.H.; Eda, G. Evolution of electronic structure in atomically thin sheets of ws₂ and wse₂. *ACS Nano* **2013**, *7*, 791–797. [CrossRef]
52. Yuan, L.; Huang, L. Exciton dynamics and annihilation in WS₂ 2D semiconductors. *Nanoscale* **2015**, *7*, 7402–7408. [CrossRef]
53. Hwang, J.D.; Chang, W.T.; Chen, Y.H.; Kung, C.Y.; Hu, C.H.; Chen, P.S. Suppressing the dark current of metal-semiconductor-metal SiGe/Si heterojunction photodetector by using asymmetric structure. *Thin Solid Films* **2007**, *515*, 3837–3839. [CrossRef]
54. Liu, D.; Wang, Q.; Shen, W.; Wang, D. Self-cleaning antireflective coating with a hierarchical texture for light trapping in micromorph solar cells. *J. Mater. Chem. C* **2017**, *5*, 103–109. [CrossRef]
55. Chang, K.; Chen, W.; Ma, L.; Li, H.; Li, H.; Huang, F.; Xu, Z.; Zhang, Q.; Lee, J.Y. Graphene-like MoS₂/amorphous carbon composites with high capacity and excellent stability as anode materials for lithium ion batteries. *J. Mater. Chem.* **2011**, *21*, 6251–6257. [CrossRef]
56. He, H.Y. Assembly of 1T-WSe₂: Sn nanosheets/graphene by a modified hydrothermal process for water splitting. *J. Sol-Gel Sci. Technol.* **2020**, *93*, 554–562. [CrossRef]
57. Xiong, M.; Qian, J.; Yang, K.; Chen, Z.; Mei, T.; Wang, J.; Li, J.; Yu, L.; Wang, X. Efficient polysulfide anchor: Brain coral-like WS₂ nanosheets. *J. Mater. Sci.* **2020**, *55*, 12031–12040. [CrossRef]
58. Ko, T.S.; Huang, C.C.; Lin, D.Y. Optical and transport properties of Ni-MoS₂. *Appl. Sci.* **2016**, *6*, 227. [CrossRef]
59. Method of Making an Integrated Photodetector in Which a Silicon Nitride Layer Forms an Anti-Reflective Film and Part of Multi-Layer Insulator within Transistor Structures. U.S. Patents US6803249B2, 12 October 2014. Available online: <https://patents.google.com/patent/US6803249B2/en> (accessed on 2 July 2020).
60. Oliva, N.; Casu, E.A.; Yan, C.; Krammer, A.; Rosca, T.; Magrez, A.; Stolichnov, I.; Schueler, A.; Martin, O.J.F.; Ionescu, A.M. van der Waals MoS₂/VO₂ heterostructure junction with tunable rectifier behavior and efficient photoresponse. *Sci. Rep.* **2017**, *7*, 14250. [CrossRef] [PubMed]
61. Basyooni, M.A.; Zaki, S.E.; Ertugrul, S.; Yılmaz, M.; Eker, Y.R. Fast response of CO₂ room temperature gas sensor based on Mixed-Valence Phases in Molybdenum and Tungsten Oxide nanostructured thin films. *Ceram. Int.* **2020**, *46*, 9839–9853. [CrossRef]
62. Tongay, S.; Zhou, J.; Ataca, C.; Liu, J.; Kang, J.S.; Matthews, T.S.; You, L.; Li, J.; Grossman, J.C.; Wu, J. Broad-range modulation of light emission in two-dimensional semiconductors by molecular physisorption gating. *Nano Lett.* **2013**, *13*, 2831–2836. [CrossRef] [PubMed]
63. Wang, Y.; Hu, X.; Guo, T.; Tian, W.; Hao, J.; Guo, Q. The competitive adsorption mechanism of CO₂, H₂O and O₂ on a solid amine adsorbent. *Chem. Eng. J.* **2021**, *416*, 129007. [CrossRef]
64. Ko, P.J.; Abderrahmane, A.; Kim, N.H.; Sandhu, A. High-performance near-infrared photodetector based on nano-layered MoSe₂. *Semicond. Sci. Technol.* **2017**, *32*, 065015. [CrossRef]

65. Wu, J.M.; Chang, W.E. Ultrahigh responsivity and external quantum efficiency of an ultraviolet-light photodetector based on a single VO₂ microwire. *ACS Appl. Mater. Interfaces* **2014**, *6*, 14286–14292. [[CrossRef](#)] [[PubMed](#)]
66. Chao, C.-H.; Weng, W.-J.; Wei, D.-H. Enhanced UV photodetector response and recovery times using a nonpolar ZnO sensing layer. *J. Vac. Sci. Technol. A Vac. Surf. Films* **2016**, *34*, 02D106. [[CrossRef](#)]
67. Liu, X.; Gu, L.; Zhang, Q.; Wu, J.; Long, Y.; Fan, Z. All-printable band-edge modulated ZnO nanowire photodetectors with ultra-high detectivity. *Nat. Commun.* **2014**, *5*, 4007. [[CrossRef](#)] [[PubMed](#)]
68. Bachmeier, A.; Hall, S.; Ragsdale, S.W.; Armstrong, F.A. Selective visible-light-driven CO₂ reduction on a p-type dye-sensitized nio photocathode. *J. Am. Chem. Soc.* **2014**, *136*, 13518–13521. [[CrossRef](#)] [[PubMed](#)]